Irradiation-induced segregation at dislocation loops in CoCrFeMnNi high entropy alloy

Wei-Ying Chen [a],[*], Jonathan D. Poplawsky [b], Yiren Chen [a], Wei Guo [b], Jien-Wei Yeh [c]

[a] *Argonne National Laboratory, Lemont IL, USA*
[b] *Oak Ridge National Laboratory, Oak Ridge TN, USA*
[c] *High Entropy Materials Center, National Tsing Hua University, Hsinchu, Taiwan*

ABSTRACT

To understand the redistribution of alloying elements in high entropy alloys under irradiation, a CoCrFeMnNi alloy was irradiated with 1 MeV Kr ions at room temperature and at 500°C, and characterized with atom probe tomography and transmission electron microscopy. At 500°C, Co and Ni were enriched around the interstitial, faulted and perfect, dislocation loops resulted from the ion irradiation. In contrast, no segregation was observed at room temperature. The inverse Kirkendall effect through vacancy flux, as opposed to the interstitial binding mechanism, was the primary underlying process attributing to the observed segregation. In addition, a ring-shaped segregation pattern was observed at the faulted dislocation loops, indicating a non-equilibrium nature of the defect clustering and solute segregation process in CoCrFeMnNi under irradiation at high temperature.

Manuscript

Radiation-induced segregation (RIS) is a non-equilibrium segregation process that takes place at point defect sinks in alloys under irradiation at elevated temperatures (0.3–0.5 T_m) [1,2]. Although it has been well accepted that the oversize and undersize solutes are depleted and enriched, respectively, at defect sinks, the understanding of RIS in complex, concentrated alloys is still challenging because of the intricate balance between competing or synergistic mechanisms [3]. Two mechanisms have profound impacts on RIS: the preferential exchange of vacancy flux with oversize elements (inverse Kirkendall effect) [4], and the preferential association of interstitial flux with undersize substitutional elements (interstitial binding) [2]. Identifying the prevailing mechanism has been the subject of many studies [1,5,6].

Recently, the RIS in high entropy alloys is of interest because the sluggish diffusion could be an effective tool to combat RIS in nuclear applications [7,8]. For austenitic Fe-Cr-Ni alloys, Allen et al. showed that the primary mechanism is the inverse Kirkendall effect [5]. For HEAs, however, the primary mechanism could be different because of their very different composition. For instance, recent study showed that the Portevin–Le Chatelier effect in HEAs cannot be satisfactorily explained with the traditional solute-pinning mechanism [9].

In regard of RIS at dislocation loops, He et al. observed the segregation of Co and Ni in CoCrFeNi, CoCrFeMnNi and CoCrFeNiPd HEAs with transmission electron microcopy (TEM) [10]. Supported by MD simulations [11,12], they suggested that the primary mechanism was interstitial binding in those HEAs. In contrast, another study by Lu et al. did not find segregation around dislocation loops in CoCrFeMnNi, and they suggested that the high lattice distortion reduced the interstitial migration, suppressing the RIS [13]. They further inferred from molecular static calculations that the segregation at faulted dislocation loops have a "disk-like" morphology, rather than a ring shape.

In this study, we used atom probe tomography (APT) and TEM to show that the inverse Kirkendall effect is the primary RIS mechanism in CoCrFeMnNi. The ranking of the degrees of segregation is generally consistent with the order of the solute size-misfit parameters. In addition, we show that the segregation at faulted dislocation loops has a "ring-like" distribution.

Equiatomic CoCrFeMnNi alloy was synthesized by arc-melting. The alloy was cold rolled by 70% and homogenized at 1200°C for 48 h with a water quench to room temperature. The alloy has a large grain size of about 400 μm and a low dislocation density of 2.6×10^{12} m⁻² [14]. The nominal and measured compositions (in atomic percent, hereafter) are given in Table 1. CoCrFeMnNi samples were electro-polished and then irradiated with 1 MeV Kr ions to a fluence of 6.3×10^{18} m⁻² at room temperature (RT) and 500°C, respectively. Before APT examination, a 100 nm Ni layer was deposited on top of the specimens to act as a fiducial for the surface using a South Bay Technologies ion beam sputtering system. Subsequently, samples were prepared using a Thermo Fisher Nova 200 focused ion beam, in which triangular prism liftouts were mounted on Si microtips and sharpened such that the long axis of the
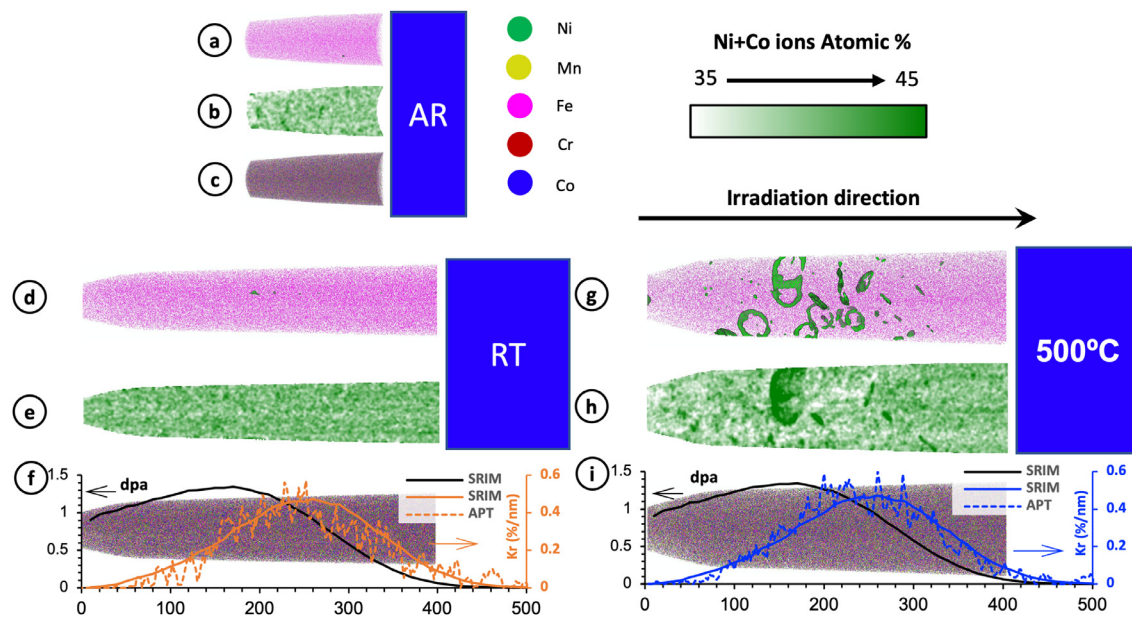
Fig. 1. APT results of CoCrFeMnNi. (a, b, c) are the as-received sample; (d, e, f) are the irradiated at RT. (g, h, i) are the irradiated at 500°C. (a, d, g) are 45% (Ni + Co) isosurfaces; (b, e, h) are 2D contour plots of Ni + Co ions; (c, f, i) are APT maps of all ions overlayed with the Kr distributions and SRIM calculations. The scales of all images are the same.
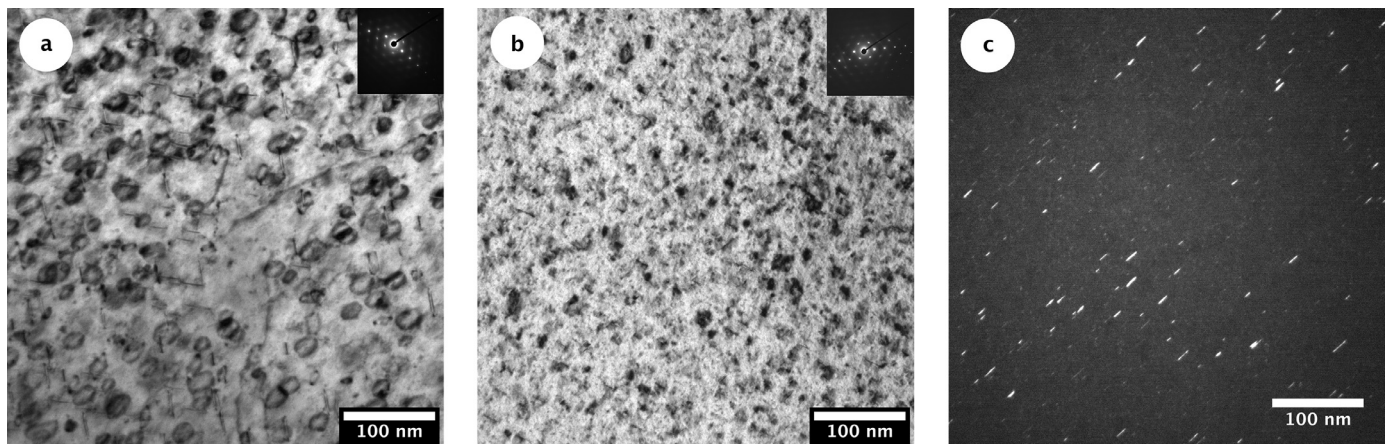

Fig. 2. Bright-field TEM images of the CoCrFeMnNi irradiated at 500°C (a) and RT (b). The imaging condition was g = 200 at the 011 zone. The insets are the corresponding diffraction patterns. (c) Same-area dark-field image of the CoCrFeMnNi irradiated at RT using the relrod streak in the diffraction pattern in (b).

Table 1
Composition and Volume Size Factors of CoCrFeMnNi.

	Ni	Co	Cr	Fe	Mn
Volume size-factor (%) [21]	0	1.76	10.34	10.57	23.2
Nominal (at. %)	20	20	20	20	20
EDS (at. %) [14]	19.8	20.8	19.8	20.4	19.3
APT (at. %)	20.0	20.0	19.7	21.1	19.2

needle was along the irradiation direction [15,16]. The APT data were acquired in a CAMECA local electrode atom probe (LEAP 4000X HR) in laser mode with a 30 K base temperature, a ~100 pJ laser power, a 0.5% detection rate, and a 200 kHz pulse repetition rate. In addition to APT, TEM was performed to characterize the dislocation loops in additional specimens irradiated to the same condition using the imaging conditions of kinematic bright-field with g = 200 and relrod dark-field at 011 zone.

Fig. 1 shows the APT results and the Kr damage and implantation distributions calculated with SRIM [17] using the quick Kinchin-Pease option [18]. The measured Kr distributions are shown in Fig. 1(f) and

Table 2
RIS Observation at dislocation loops in CoCrFeMnNi.

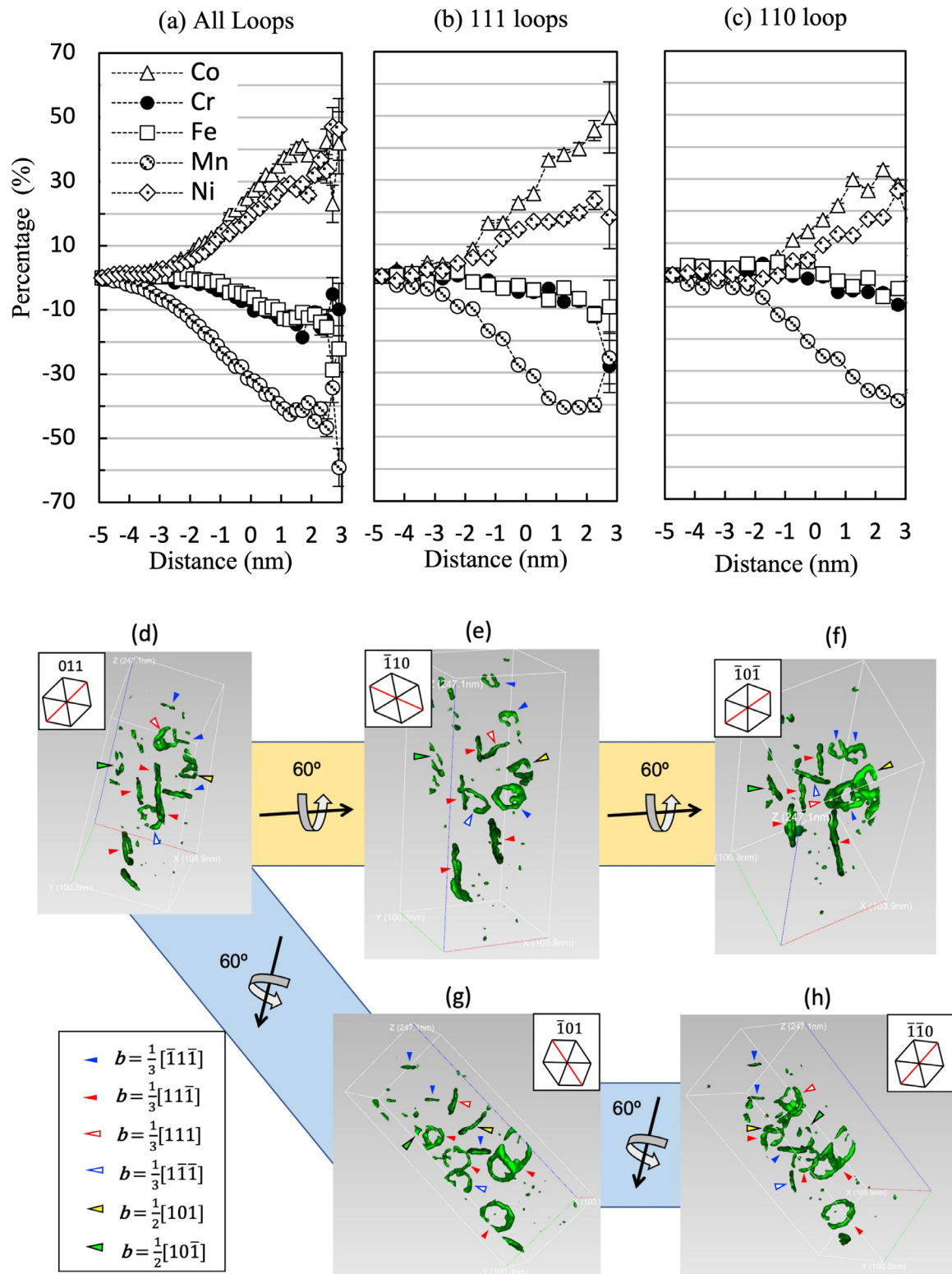| Irradiation Condition	Observation	Ref.
1 MeV Kr ions at 500°C	Enriched with Ni and Co. Depleted with Mn, Cr and Fe	This work
1250 eV electrons at 400°C	Enriched with Co. Depleted with Mn.	[10]
3 MeV Ni ions at 500°C	No segregation	[13]

Fig. 3. The proxigram of (a) all dislocation loops, (b) a 111 loop and (c) a 110 loop in the CoCrFeMnNi irradiated with 1 MeV Kr at 500°C. (d-h) The 45% (Ni+Co) isosurfaces of 111 loops and 110 loops viewed from different angles. The insets show the corresponding crystallographic orientations where the red lines indicate the {200} planes.

Fig. 1(i) for RT and 500°C, respectively, overlaying on the corresponding all-ions maps. It shows that the measured Kr implantation profiles agree well with the SRIM calculations, and that the whole implantation ranges were captured in both APT specimens.

As shown in Fig. 1, the three specimens were analyzed with 2D contour plots and iso-concentration surfaces (isosurfaces). For the irradiated specimens, the Kr beam direction is from left to right, and the left edges of the APT images correspond to the irradiated surfaces. The 2D contour plots were taken with 5 nm slices, showing a combined concentration of Ni and Co between 35 to 45%, as the nominal combined concentration of Ni and Co is 40%. The isosurfaces correspond to a combined Ni+Co concentration of 45%. No segregation was observed in the as-received and RT-irradiated specimens as shown in Fig. 1(a, b, d, e).

In contrast, as shown in Fig. 1(g, h), the 500°C specimen clearly shows Ni and Co-enriched loops with a morphology consistent with the dislocation loops observed with TEM as shown in Fig. 2(a). The loops were observed in between 80 nm and 350 nm below the irradiated surface, coinciding with the high-dpa regions calculated by SRIM. Supplemental Video 1 shows the isosurfaces in 3D. No loops were observed near the irradiation surface because mobile interstitials were depleted near the surface [19].

The elemental segregation at dislocation loops was quantitatively investigated using proximity histogram (proxigram). The proxigram was then converted from their absolute concentration to the relative concentration change by calculating $((C_i(x) - C_{i,M})/C_{i,M})\times100\%$. The $C_i(x)$ is the concentration of element i at a distance of x from the isosurface of Ni+Co = 45%. The $C_{i,M}$ is the concentration of element i in the matrix. A positive x corresponds to the direction toward the dislocation loops. As shown in Fig. 3(a), the concentrations of Co and Ni increase significantly at the dislocation loops. In contrast, the concentrations of Fe, Cr and Mn all decrease near the dislocation loops with Mn depleting the most. Similarly, a recent study also showed Ni and Co enrichment around the irradiation-induced voids in some NiCo-containing multicomponent alloys [20]. In addition, our APT result is partially consistent with the TEM observation by He et al., in which Co enrichment and Mn depletion were observed in a CoCrFeMnNi alloy irradiated with 1250 keV electrons at 400°C [10]. Neither Ni enrichment nor Fe and Cr depletion can be evidently observed in their study. Nevertheless, both this work and He's results differ from the TEM observation by Lu et al. where no segregation at dislocation loops was observed in a CoCrFeMnNi alloy irradiated with 3 MeV Ni ions at 500°C [13]. A summary of these results is given in Table 2.

In addition, He et al. reported similar segregation at 1/3<111> Frank faulted loops and 1/2 <110> perfect loops in CoCrFeMnNi by TEM examination [10]. For APT, determining the loop type is not straight forward because of the lacking crystallographic information after irradiation. In order to determine the loop type, the 45% (Ni+Co) isosurfaces in Fig. 1(g) were viewed from different angles. As shown in Fig. 3(d), two sets of loops having an edge-on orientations with respect to the page surface are indicated by the solid red and solid blue arrows. The angle between the two sets of loops is close to 70.5°, which matches the angle between two edge-on 1/3<111> loops. If we assume the direction perpendicular to the page surface shown in Fig. 3(d) is parallel to the 011 zone axis, these two sets of edge-on loops are b = 1/3 [11$\bar{1}$] and 1/3 [$\bar{1}$1$\bar{1}$], respectively. With a 3D viewer, the APT result is rotated about the [11$\bar{1}$] axis by 60° to the $\bar{1}$10 zone, and by 120° to the $\bar{1}$0$\bar{1}$ zone as shown, respectively, in Fig. 3(e) and Fig. 3(f). Similarly, the APT result can be rotated about the [$\bar{1}$1$\bar{1}$] axis by 60° to the $\bar{1}$01 zone and by 120° to the $\bar{1}$10 zone as shown, respectively, in Fig. 3(g) and Fig. 3(h). As a result, all loops can be indexed consistently as Frank loops laying on {111} planes and perfect loops on {110} planes, verifying the initial assumption of the 011 zone for Fig. 3(d). Ten loops were identified as Frank loops, as indicated with red and blue arrows, while two loops were identified as perfect loops as indicated with green and yellow arrows. The proxigrams of one Frank loop and one perfect loop are shown in Fig. 3(b) and 3(c), respectively. They show that the segregation at the
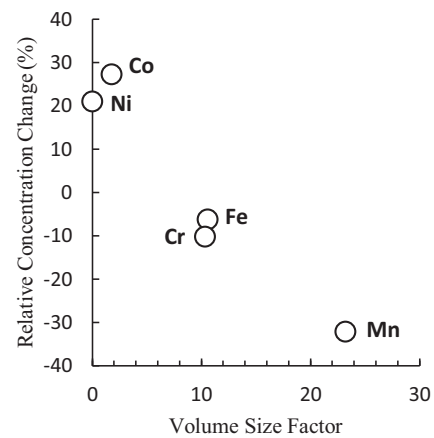

Fig. 4. The relative concentration change of individual elements measured at the Ni + Co = 45% isosurfaces as a function of their volume size factor.

Frank loops and perfect loops is evidently similar, which confirms the TEM observation by He et al [10].

The segregation of solute elements is associated with the relative atomic sizes of solutes with respect to the matrix, no matter it is interstitial-controlled or vacancy-controlled. Okamoto and co-workers have showed that the oversize and undersize solutes are depleted and enriched, respectively, at defect sinks [1,2]. The volume size factor (VSF) of a solute is defined as the fractional molar volume change per unit change in concentration of solute. Table 1 lists the VSF of each element in the Ni matrix reported by King [21]. Based on the APT observation in Fig. 3, the ranking of atom sizes should be Mn > Cr ≳ Fe > Ni ≳ Co. The order of VSF, being Mn > Fe ≳ Cr > Co ≳ Ni, generally agree with the expected order from RIS observation, while the rankings between Fe and Cr, and between Co and Ni are inversed. Note that the VSF difference between Fe and Cr, and between Co and Ni are small, which correspond to their small RIS difference. Nevertheless, as shown in Fig. 4 a general trend can be seen that the enrichment decreases, and depletion increases, with increasing VSF. The slight departure from the sole dependence of RIS on VSF indicates that there are secondary effects possibly from the enthalpy of mixing and electronegativity [10,22]. In addition, the VSF measured by King [21] was on binary alloys. The VSF of elements in CoCrFeMnNi may deviate due to the complex energy landscape of high entropy alloys [23].

Fig. 5 shows 2D concentration contour plots of a faulted loop with its plane on the page. Fig. 5(a) is a lower magnification Mn map while Fig. 5(b) to (f) shows magnified maps of the five elements. The color scale is adjusted in each figure. Fig. 5(a) shows that the concentration becomes close to the matrix concentration at roughly 6 nm away from the dislocation core, which is consistent with the proxigrams in Fig. 3. The magnified plots in Fig. 5(b)-(f) show that the segregation is notably concentrated at the dislocation core of the loop. Mn depletes, while Co and Ni enrich around the loop. Fe and Cr also slightly deplete.

Based on a study by Lu et al. [13], a "disk-shaped" segregation distribution (opposed to a "ring-shaped" distribution) is energetically favorable around Frank loops . However, as evidenced in Fig. 5 and the isosurfaces in Fig. 1, the segregated elements are distributed along the edge of the loop, forming a "ring-shaped" pattern. The disagreement between the APT observation and the strain energy calculation indicates that the dynamic process of solute migration interacting with point defects needs to be considered.

Fig. 2(a) shows the TEM observation of the CoCrFeMnNi irradiated at 500°C to the same dose. Consistent with the APT observation, irradiated microstructure revealed by TEM consists of interstitial dislocation loops with an average size of 19 nm and a density of 9.7×10^{21} m^{-3} [19]. The ratio between faulted Frank loops and perfect loops is roughly 3:1. This microstructure is similar to that of Type 316 stainless steel irradiated
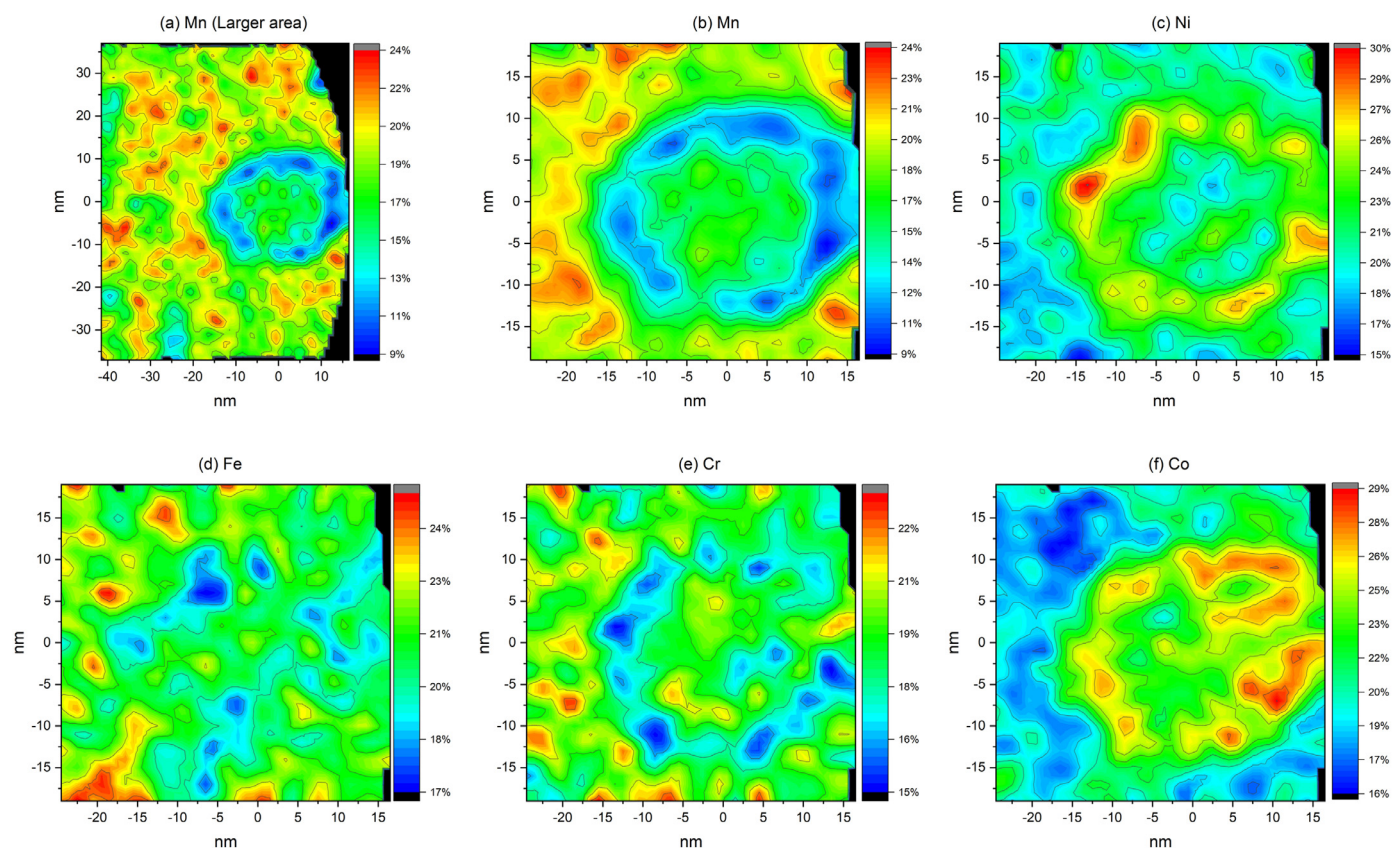
Fig. 5. 2D concentration contours showing the elemental distribution of each element on the plane of a faulted dislocation loop.

at an annealing temperature stage V (>∼300°C) where vacancy clusters become thermally unstable and start to emit vacancies [24,25].

On the other hand, as shown in Fig. 2(b), the microstructure of the CoCrFeMnNi irradiated at RT is similar to that of Type 316 stainless steel irradiated below the stage III annealing temperature (∼<50°C) where the vacancy mobility is insignificant [26]. At RT, the dominant microstructure is a high density of small defect clusters directly created by cascade quench, appearing as uniform "black spots" in the image [25]. As compared with the 500°C sample, the defect density in the RT sample was significantly higher, and the defect size was significantly smaller, which is qualitatively consistent with a recent observation on a CrFeMnNi neutron-irradiated at RT [27]. Nevertheless, larger dislocation loops greater than 10 nm were still observed as shown in the same-area relrod dark-field image in Fig. 2(c). The relrod dark-field image reveals one out of the four sets of Frank loops on {111} planes. Previous studies indicate that nearly all faulted loops larger than 10 nm in austenitic stainless steels are interstitial loops [25].

At RT, the interstitials are mobile, but not vacancies. The presence of large interstitial dislocation loops in the CoCrFeMnNi irradiated at RT manifests the long-distance migration of interstitials. The lack of RIS at RT therefore indicates that an interstitial-driven RIS mechanism is not operational in CoCrFeMnNi. In other words, there is no observable association of alloy elements with interstitials migration toward dislocation loops. In contrast, at 500°C, both interstitials and vacancies are mobile. The APT observation of RIS at 500°C was due to the vacancy flux toward dislocation loops associating with preferred elements. Combining the TEM and APT results, it can be inferred that the RIS at interstitial dislocation loops in the CoCrFeMnNi is attributed to the inverse Kirkendall effect through vacancies, which also suggests that the framework developed by Allen et al. [5] on austenitic Fe-Cr-Ni alloys can be extended to CoCrFeMnNi. The diffusivity of the elements should follow the order of Mn > Cr ≳ Fe > Ni ≳ Co based on the degree of enrichment

or depletion of these elements at dislocation loops, which is closely similar to the order of vacancy migration energy recently reported by Choi et al. [28]: Mn < Fe < Cr < Co ≲ Ni. The slower diffusers, Co and Ni, enriched. The faster diffusers, Mn, depleted at dislocation loops. In addition, the diffusivities of Fe and Cr were higher than the average, and they also depleted.

In summary, this study reveals a complex redistribution of the elements in the CoCrFeMnNi alloy under ion irradiation. An enrichment of Ni and Co, and a depletion of Mn, Cr, and Fe have been observed at interstitial dislocation loops at 500°C, but not at RT. Both APT and TEM observations lead to a conclusion that the inverse Kirkendall effect through vacancy flux, as opposed to the interstitial-binding, is the primary mechanism for RIS in HEAs. The extent of depletion/enrichment of an individual element is closely related to its VSF and migration energy. This improved understanding on the RIS in HEAs is important for the potential applications of HEAs in nuclear environment.

Declaration of Competing Interest

The authors declare that they have no known competing financial interests or personal relationships that could have appeared to influence the work reported in this paper.

Acknowledgements

Supplementary materials

Supplementary material associated with this article can be found, in the online version, at doi:10.1016/j.mtla.2020.100951.

References

[1] P.R. Okamoto, L.E. Rehn, Radiation-induced segregation in binary and ternary alloys, J, Nucl. Mater. 83 (1979) 2–23, doi:10.1016/0022-3115(79)90587-7.

[2] P.R. Okamoto, H. Wiedersich, Segregation of alloying elements to free surfaces during irradiation, J, Nucl. Mater. 53 (1974) 336–345, doi:10.1016/0022-3115(74)90267-0.

[3] A.J. Ardell, P. Bellon, Radiation-induced solute segregation in metallic alloys, Curr. Opin. Solid State Mater. Sci. 20 (2016) 115–139, doi:10.1016/j.cossms.2015.11.001.

[4] A.D. Marwick, Segregation in irradiated alloys: the inverse Kirkendall effect and the effect of constitution on void swelling, J, Phys. F Met. Phys. 8 (1978) 1849–1861, doi:10.1088/0305-4608/8/9/008.

[5] T.R. Allen, J.T. Busby, G.S. Was, E.A. Kenik, On the mechanism of radiation-induced segregation in austenitic Fe-Cr-Ni alloys, J, Nucl. Mater. 255 (1998) 44–58, doi:10.1016/S0022-3115(98)00010-5.

[6] H. Wiedersich, P.R. Okamoto, N.Q. Lam, A theory of radiation-induced segregation in concentrated alloys, J, Nucl. Mater. 83 (1979) 98–108, doi:10.1016/0022-3115(79)90596-8.

[7] N.A.P.K. Kumar, C. Li, K.J. Leonard, H. Bei, S.J. Zinkle, Microstructural stability and mechanical behavior of FeNiMnCr high entropy alloy under ion irradiation, Acta Mater 113 (2016) 230–244, doi:10.1016/j.actamat.2016.05.007.

[8] K.-Y. Tsai, M.-H. Tsai, J.-W. Yeh, Sluggish diffusion in Co–Cr–Fe–Mn–Ni high-entropy alloys, Acta Mater 61 (2013) 4887–4897, doi:10.1016/J.ACTAMAT.2013.04.058.

[9] C.W. Tsai, C. Lee, P.T. Lin, X. Xie, S. Chen, R. Carroll, M. Leblanc, B.A.W. Brinkman, P.K. Liaw, K.A. Dahmen, J.W. Yeh, Portevin-Le Chatelier mechanism in face-centered-cubic metallic alloys from low to high entropy, Int. J. Plast. 122 (2019) 212–224, doi:10.1016/j.ijplas.2019.07.003.

[10] M.-R. He, S. Wang, S. Shi, K. Jin, H. Bei, K. Yasuda, S. Matsumura, K. Higashida, I.M. Robertson, Mechanisms of radiation-induced segregation in CrFeCoNi-based single-phase concentrated solid solution alloys, Acta Mater 126 (2017) 182–193, doi:10.1016/J.ACTAMAT.2016.12.046.

[11] D.S. Aidhy, C. Lu, K. Jin, H. Bei, Y. Zhang, L. Wang, W.J. Weber, Point defect evolution in Ni, NiFe and NiCr alloys from atomistic simulations and irradiation experiments, Acta Mater 99 (2015) 69–76, doi:10.1016/J.ACTAMAT.2015.08.007.

[12] Y.N. Osetsky, L.K. Béland, R.E. Stoller, Specific features of defect and mass transport in concentrated fcc alloys, Acta Mater 115 (2016) 364–371, doi:10.1016/j.actamat.2016.06.018.

[13] C. Lu, T. Yang, K. Jin, N. Gao, P. Xiu, Y. Zhang, F. Gao, H. Bei, W.J. Weber, K. Sun, Y. Dong, L. Wang, Radiation-induced segregation on defect clusters in single-phase concentrated solid-solution alloys, Acta Mater 127 (2017) 98–107, doi:10.1016/J.ACTAMAT.2017.01.019.

[14] W.-Y. Chen, X. Liu, Y. Chen, J.-W. Yeh, K.-K. Tseng, K. Natesan, Irradiation effects in high entropy alloys and 316H stainless steel at 300 °C, J, Nucl. Mater. 510 (2018) 421–430, doi:10.1016/J.JNUCMAT.2018.08.031.

[15] M. Li, M.K. Miller, W.-Y. Chen, Phase stability in thermally-aged CASS CF8 under heavy ion irradiation, J, Nucl. Mater. 462 (2015) 214–220, doi:10.1016/J.JNUCMAT.2015.03.034.

[16] K. Thompson, D. Lawrence, D.J. Larson, J.D. Olson, T.F. Kelly, B. Gorman, In situ site-specific specimen preparation for atom probe tomography, Ultramicroscopy 107 (2007) 131–139, doi:10.1016/j.ultramic.2006.06.008.

[17] J.F. Ziegler, M.D. Ziegler, J.P. Biersack, SRIM - The stopping and range of ions in matter (2010), Nucl. Instruments Methods Phys. Res. Sect. B Beam Interact. Mater. Atoms. 268 (2010) 1818–1823, doi:10.1016/j.nimb.2010.02.091.

[18] R.E. Stoller, M.B. Toloczko, G.S. Was, A.G. Certain, S. Dwaraknath, F.A. Garner, On the use of SRIM for computing radiation damage exposure, Nucl. Instrum. Methods Phys. Res. Sect. B Beam Interact. with Mater. Atoms 310 (2013) 75–80, doi:10.1016/J.NIMB.2013.05.008.

[19] W.-Y. Chen, M.A. Kirk, N. Hashimoto, J.-W. Yeh, X. Liu, Y. Chen, Irradiation effects on Al0.3CoCrFeNi and CoCrMnFeNi high-entropy alloys, and 316H stainless steel at 500 °C, J, Nucl. Mater. 539 (2020) 152324, doi:10.1016/j.jnucmat.2020.152324.

[20] X. Wang, C. Hatzoglou, B. Sneed, Z. Fan, W. Guo, K. Jin, D. Chen, H. Bei, Y. Wang, W.J. Weber, Y. Zhang, B. Gault, K.L. More, F. Vurpillot, J.D. Poplawsky, Interpreting nanovoids in atom probe tomography data for accurate local compositional measurements, Nat. Commun. 11 (2020) 1–11, doi:10.1038/s41467-020-14832-w.

[21] H.W. King, Quantitative size-factors for metallic solid solutions, 1966.

[22] F. Otto, Y. Yang, H. Bei, E.P. George, Relative effects of enthalpy and entropy on the phase stability of equiatomic high-entropy alloys, Acta Mater. 61 (2013) 2628–2638, doi:10.1016/j.actamat.2013.01.042.

[23] Y. Zhang, G.M. Stocks, K. Jin, C. Lu, H. Bei, B.C. Sales, L. Wang, L.K. Béland, R.E. Stoller, G.D. Samolyuk, M. Caro, A. Caro, W.J. Weber, Influence of chemical disorder on energy dissipation and defect evolution in concentrated solid solution alloys, Nat. Commun. 6 (2015) 8736, doi:10.1038/ncomms9736.

[24] D.J. Edwards, E.P. Simonen, F.A. Garner, L.R. Greenwood, B.M. Oliver, S.M. Bruemmer, Influence of irradiation temperature and dose gradients on the microstructural evolution in neutron-irradiated 316SS, J, Nucl. Mater. 317 (2003) 32–45, doi:10.1016/S0022-3115(03)00003-5.

[25] S.J. Zinkle, P.J. Maziasz, R.E. Stoller, Dose dependence of the microstructural evolution in neutron-irradiated austenitic stainless steel, J, Nucl. Mater. 206 (1993) 266–286, doi:10.1016/0022-3115(93)90128-L.

[26] C. Dimitrov, A. Benkaddour, O. Dimitrov, C. Corbel, P. Moser, Point Defects in FCC Fe-Cr-Ni Alloys,, in: Vacanc. Interstitials Met. Alloy., Trans Tech Publications Ltd, 1987, pp. 1275–1280, doi:10.4028/www.scientific.net/MSF.15-18.1275.

[27] C. Li, X. Hu, T. Yang, N.K. Kumar, B.D. Wirth, S.J. Zinkle, Neutron irradiation response of a Co-free high entropy alloy, J. Nucl. Mater. 527 (2019) 151838, doi:10.1016/j.jnucmat.2019.151838.

[28] W.M. Choi, Y.H. Jo, S.S. Sohn, S. Lee, B.J. Lee, Understanding the physical metallurgy of the CoCrFeMnNi high-entropy alloy: An atomistic simulation study, Npj Comput. Mater. 4 (2018) 1–9, doi:10.1038/s41524-017-0060-9.